Time-varying global energy budget since 1880 from a new reconstruction of ocean warming

Article

Accepted Version

Time-varying global energy budget since 1880 from a new reconstruction of ocean warming

Quran Wu[a,1], **Jonathan M. Gregory**[a,b], **Laure Zanna**[c], **and Samar Khatiwala**[d]

This manuscript was compiled on March 5, 2025

The global energy budget is fundamental for understanding climate change. It states that the top-of-atmosphere imbalance between radiative forcing (which drives climate change) and radiative response (which resists the forcing) equals energy storage in Earth's heat reservoirs (i.e. the ocean, atmosphere, land and cryosphere). About 90% of Earth's energy imbalance is stored as heat content in the ocean interior, which is poorly sampled before 1960. Here, we reconstruct Earth's energy imbalance since 1880 by inferring subsurface ocean warming from surface observations via a Green's function approach. Our estimate of Earth's energy imbalance is consistent with the current best estimates of radiative forcing and radiative response during 1880–2020. The consistency is improved in this study compared to previous ones. We find two distinct phases in the global energy budget. In 1880–1980, Earth's energy imbalance closely followed the radiative forcing. After 1980, however, Earth's energy imbalance increased at a slower rate than the forcing; in 2000–2020, the imbalance amounted to less than 50% of the forcing. In simulations of historical climate change, the model-mean energy imbalance is consistent with observations within uncertainties, but individual models with a "weak" response to anthropogenic aerosol agree better with observations than those with a "strong" response. Because the global energy budget before and after 1980 imply very different global warming in the future, further studies are required to better understand the cause of this historical variation.

global energy budget | ocean heat uptake | radiative forcing | radiative response | climate model

Significance Statement

The global energy budget is essential for understanding human-induced climate change. It states that energy storage in Earth's heat reservoirs is determined by the top-of-atmosphere imbalance between radiative forcing (which drives climate change) and radiative response (which resists the forcing). Here, we infer Earth's energy imbalance from a new reconstruction of ocean warming. This improves the closure of the global energy budget for 1880–2020 compared to previous studies. We find two distinct phases in the global energy budget. Earth's energy imbalance closely followed the forcing in 1880–1980, but was less than half of the forcing in 2000–2020. That is: the fraction of forcing that went into heating the Earth has been smaller in recent decades than in earlier periods.

The global energy budget is a fundamental aspect of Earth's climate system. Human-induced changes in the atmospheric composition have resulted in a positive radiative forcing F at the top of the atmosphere (TOA) since 1750, which warms the Earth's surface (1, 2). A warmer Earth tends to radiate more energy to space, counteracting the effect of F; this is referred to as Earth's radiative response R (3). The imbalance between F and R determines the net TOA radiative flux, which must be equal to N, the change in Earth's heat storage (4), as required by energy conservation, i.e. $N = F + R$. Reproducing the historical global energy budget is a basic test for climate models. The energy budget itself provides a useful constraint on the Earth's equilibrium temperature response to CO_2 forcing (3, 5, 6).

The global energy budget has been analysed using observation-based data (2, 7–9). Earth's energy imbalance N can be derived from observed changes in Earth's heat reservoirs. During 1971–2020, observations suggest that about 90% of N is stored in the ocean, followed by 6% in the ground, 4% in the cryosphere and 1% in the atmosphere (4, 10). From 2000 onwards, satellite radiometers have provided a direct estimate of N, which agrees well with the N inferred from Earth's heat storage (11). In contrast, the radiative forcing F and the radiative response R are not observable directly. F can be derived from radiative transfer models forced with observed changes in the atmospheric composition. R can be calculated as the product of the observed global surface warming T and the climate feedback parameter α, with the caveat that α exhibits a large uncertainty in the literature (2). The fifth assessment report of the Intergovernmental Panel on Climate Change (IPCC) demonstrated that the global energy budget is closed within uncertainties during 1971–2010 (8). The IPCC sixth assessment report extended this analysis to 2018 with improved consistency (2).

Global ocean heat content (OHC) change (unit: J) is an important measure of Earth's energy imbalance N (unit: W m^{-2}) stored in the ocean, i.e. $\mathrm{dOHC}/\mathrm{d}t \approx 90\% \times N \times A$, where A is the Earth's surface area. Conventionally, OHC estimates are derived from mapping in-situ temperature data to a global ocean grid ("in-situ" means that data is collected at the point where the instrument is located). The historical temperature data are sparse in space and time and suffer from systematic instrument biases, especially during early periods (12, 13). This has prevented an

Author affiliations: [a]National Centre for Atmospheric Science, University of Reading, Reading, UK; [b]Met Office Hadley Centre, Exeter, UK; [c]Courant Institute, New York University, New York, USA; [d]School of International Liberal Studies, Waseda University, Tokyo, Japan

Q.W. and J.M.G. designed research; Q.W. performed research; L.Z. and S.K. contributed new analytic tools; Q.W., J.M.G., L.Z. and S.K. wrote the paper.

The authors declare no competing interests.

[1]To whom correspondence should be addressed. E-mail: quran.wu@reading.ac.uk

estimate of global OHC change before 1960, which leaves a gap in the global energy budget record. Since 2006, Argo autonomous floats have provided high-quality temperature measurements with unprecedented spatial coverage of the global ocean, greatly improving the accuracy of the OHC estimate (14).

Recently, methods have been developed for reconstructing OHC before 1960 (15, 16). In particular, Zanna et al. (16) estimated OHC change starting from 1870 by propagating observed sea surface temperatures (SSTs) into the ocean interior using a Green's function (GF) approach (17–19).

In this study, we derive Earth's energy imbalance N since 1880 from an OHC reconstruction based on an improved GF approach. Our estimate of Earth's energy imbalance N agrees with the sum of radiative forcing F and radiative response R derived from independent sources. This allows us to present a continuous record of the global energy budget starting from 1880 using observation-based data.

Green's Function Method in a Nutshell

In this section, we explain the procedure of computing OHC change and associated uncertainties using the GF method. The GF method is detailed in Materials and Methods (MM) A and contrasted with the in-situ method in Table 1.

Ocean heat uptake (OHU) is caused by surplus heat being added to the ocean surface via air-sea fluxes and then carried to depth by ocean transport (advection and mixing). The GF method exploits this fact and attempts to reconstruct ocean warming at depth from its surface signature. For a given interior location, the GF estimate of ocean warming can be written as

$$\Theta_{\mathrm{e}}(t) = \sum_{\mathbf{r}_{\mathrm{s}}} \sum_{t_{\mathrm{s}}<t} G(\mathbf{r}_{\mathrm{s}}, t-t_{\mathrm{s}}) \Theta_{\mathrm{e}}^{\mathrm{s}}(\mathbf{r}_{\mathrm{s}}, t_{\mathrm{s}}), \qquad [1]$$

where Θ_{e} and $\Theta_{\mathrm{e}}^{\mathrm{s}}$ are the interior and surface ocean temperature change relative to a pre-industrial state, respectively, t and t_{s} their corresponding time variables, and $\mathbf{r}_{\mathrm{s}}$ (longitude and latitude) the location vector of $\Theta_{\mathrm{e}}^{\mathrm{s}}$. Basically, $\Theta_{\mathrm{e}}(t)$ is reconstructed as the weighted sum of the $\Theta_{\mathrm{e}}^{\mathrm{s}}$ values everywhere at the ocean surface and any time prior to t, with the GF kernel G providing the weightings. Physically, the GF kernel partitions a water parcel at a given location according to the time and place of its last surface contact; i.e. the joint water-mass and transit-time distribution (17, 19). Importantly, the GF method does not rely on subsurface temperature measurements, in contrast to the in-situ method (Table 1).

The GF method requires two inputs: the GF kernel G and the boundary condition $\Theta_{\mathrm{e}}^{\mathrm{s}}$. These are derived as follows.

The GF kernel G is derived from observations of ocean transient tracers CFC-11 and CFC-12 via an inverse approach, using simulations of G as an initial guess (18, 20) (MM B). This method exploits the fact that the GF is an intrinsic property of ocean circulation (advection and mixing) and thus applies to any conservative tracer in the ocean.

The GF derived here has two caveats. First, CFC observations only constrain G for lead times less than ~50 years because CFC emissions started in the 1950s. We expect this caveat has little impact on our result because we focus on historical climate change, which is dominated by responses on multi-decadal timescales (21). While tracers such as argon-39 can further constrain G on centennial timescales, very few measurements are available (22). Second, we assume G is stationary in time because observations are insufficient to constrain its time evolution. That is, we ignore potential changes in ocean circulation under global warming, which may lead to a roughly 10% overestimate of global OHC increase between 2008 and 1980 (16, 23).

Technically, the boundary condition $\Theta_{\mathrm{e}}^{\mathrm{s}}$ should be surface excess temperature (23). By that we mean the part of SST change that originates at the surface, excluding SST redistribution due to changes in ocean circulation. Because $\Theta_{\mathrm{e}}^{\mathrm{s}}$ is not observable, we construct it by combining observations and model simulations (MM C). We separate $\Theta_{\mathrm{e}}^{\mathrm{s}}$ into the global mean and regional anomalies. The former is derived from the global-mean SST change in observations, while the latter are diagnosed from climate model simulations. Deriving the global-mean $\Theta_{\mathrm{e}}^{\mathrm{s}}$ from the global-mean SST change introduces a cold bias because the latter contains a weak cooling signal from SST redistribution (MM C). This leads to an underestimate of global OHC increase, which partly compensates the overestimate due to G discussed earlier.

We differ from Zanna et al. (16) in that we impose observational constraints on the GF kernel and we use a different construction of boundary conditions (Table 1). These changes bring the GF OHC estimate closer to the in-situ estimate during the Argo period (shown later).

We quantify the uncertainty of the GF OHC estimate using sets of alternative estimates of the GF kernel G and the boundary condition $\Theta_{\mathrm{e}}^{\mathrm{s}}$. We derive twelve G estimates from three first-guess solutions and four realisations of ocean tracer observations (MM B). We also derive six $\Theta_{\mathrm{e}}^{\mathrm{s}}$ estimates from three observational SST datasets and two excess temperature simulations (MM C). In total, our sensitivity test produces $12 \times 6 = 72$ members of the GF OHC estimate. Results are reported as the ensemble mean $\pm$ 2 $\times$ standard deviation (σ). Uncertainties from other studies are converted to the 2σ-range when discussed here, assuming a Gaussian error distribution.

SST datasets have two potential biases in early periods: a cold excursion in 1900–1920 and the World War 2 warm anomaly in 1939–1945 (24–28). To examine how these biases affect the GF OHC estimate qualitatively, we apply the following simple corrections. We remove the 1900–1920 cold excursion by setting SST anomaly in that period to its 1880–1900 time mean, and remove the 1939–1945 warm anomaly by scaling down SST anomaly in that period by 50% (i.e. a reduction of 0.15 K). In both case, the anomaly is relative to the 1870–1880 time mean. The bias corrections and the resulting differences in our OHC estimate are shown in Fig. S5. In what follows, we focus on the results with the bias corrections and discuss the differences that arise without them when relevant.

Global Ocean Heat Uptake

In this section, we compare the GF OHC estimate of this study against (i) the in-situ OHC estimates of Cheng (31), Levitus (32), Ishii (33) and Bagnell (34) and (ii) the GF OHC estimates of Zanna (16) and Gebbie (15). The results of Cheng, Levitus, Ishii are shown in Fig. 1, while those of

Table 1. A comparison of different methods for estimating ocean heat uptake

Method	Green's function G	boundary condition Θ_e^s	subsurface temperature measurements
This study	observation-based, constrained by CFC-11 and CFC-12 in the ocean, initial guesses are derived from ocean models	SST anomaly relative to 1870–1880 + corrections for a) excess temperature, b) the 1900–1920 cold excursion, and c) the World War 2 warm anomaly	not used
Zanna (16)	derived from an ocean state estimate (29)	SST anomaly relative to 1870–1880	not used
Gebbie (15)	observation-based, inferred from climatology of ocean tracers (30)	SST anomaly relative to 0015	not used
In situ	N/A	N/A	XBT, CTD, Argo, etc.

Bagnell and Gebbie are shown separately in Fig. S6 for clarity. All of them are integrated over the upper 2000 m.

Ocean Heat Content Change. The GF OHC estimate of this study exhibits an upward trajectory during the historical period (Fig. 1a). The global OHC change between 2006–2015 and 1956–1965 is 265±142 ZJ from our estimate (black dot, Fig. 1b, leftmost column), 230±38 ZJ from Levitus (blue dot) and 258±54 ZJ from Cheng (green dot), for instance; other OHC estimates are consistent with those numbers within uncertainties (Figs. 1b and S6b). 1956–1965 is a common starting period for the in-situ datasets.

Different choices of SST dataset and excess temperature estimate (MM C) result in a ±110 ZJ (±2σ) spread in the GF OHC change between 2006–2015 and 1956–1965 (Fig. 1b, rightmost column), while the corresponding spread due to uncertainties in the GF kernel is ±85 ZJ (Fig. 1b, middle column). The latter arises because existing observations are insufficient to fully constrain the GF kernel.

Ocean Heat Uptake Rate. We evaluate the rate of OHU (i.e. its time-derivative) using linear trends derived from a 20-year moving window, and express the result per unit area of Earth surface. The choice of 20 years for the window is a compromise between filtering out the unforced variability and resolving the time evolution. Altering the window span from 20 years to 10, 15 or 30 years does not affect the time evolution of the OHU rate in Fig. 1 very much, although a longer window does give a smoother timeseries (Fig. S7). The uncertainty of the in-situ OHU rate has been assessed in the literature using different methods, as summarised in Meyssignac et al. (10) table 1. We use the 1993–2008 error of ±0.13 W m^{-2} in Lyman et al. (35) as the 2σ-error of the in-situ OHU rate, because it accounts for a comprehensive list of uncertainties. In addition, we assume that the in-situ error of ±0.13 W m^{-2} is constant in time. We note that this choice likely underestimates the in-situ error before the 1990s (36), but using a larger in-situ error does not affect our discussion below.

The OHU rate has exhibited a robust acceleration since the 1960s (36–38). The GF OHU rate (this study) increased from 0.12±0.23 W m^{-2} in 1960–1980 to 0.63±0.23 W m^{-2} in 2000–2020 (Fig. 1c, black line), i.e. a linear trend of 0.12±0.07 W m^{-2} per decade over 1960–2020. The Cheng estimate shows a similar OHU rate increase over the same period, from 0.10±0.13 W m^{-2} to 0.60±0.13 W m^{-2}. The in-situ OHU rates may be underestimated before 1990 because of linear vertical interpolation and the XBT data biases (39). The in-situ OHU rates differ from one another regarding detailed time evolution, but the difference is not significant considering their uncertainties (±0.13 W m^{-2}). The Zanna OHU rate exhibits a weaker upward trend than the in-situ estimates in 1980–2020, while the Gebbie OHU rate exhibits a downward trend after 1990 (Figs. 1c and S6c). Note that the Gebbie estimate was built to study OHU on a much longer timescale than the one focused here (past 2000 years vs. past 140 years).

Prior to 1960, the GF estimate (this study) suggests that the OHU rate was accelerating in 1920–1940 (central years), and decelerating in 1950–1970 (Fig. 1c, black line). The transition between the two episodes coincides with the ramp-up of anthropogenic aerosol emission (40, 41).

The potential biases in SST datasets have a marked impact on the GF OHU rate prior to 1960 (Fig. 1c compare the black solid and dashed line). Removing the cold excursion in 1900–1920 changes the OHU rate in 1900 from -0.21±0.19 to 0.06±0.12 W m^{-2}. Halving the World War 2 warm anomaly reduces the OHU rate in 1940 from 0.47±0.19 to 0.31±0.17 W m^{-2}. Whether the above bias corrections can be justified is examined later through the lens of the global energy budget. The Zanna and Gebbie estimates both show a reversal in the trend of OHU rate between 1920–1940 and 1950–1970, similar to our estimate (Fig. S6c). However, the peak OHU rate at 1940 is higher in their estimates compared to ours; this difference is potentially related to the World War 2 SST biases discussed above.

The Argo Era. We compare the OHU rate from different estimates for 2006–2020, when the Argo floats have achieved a near-global coverage in 0–2000 m. During 2006–2020, the GF estimate (this study) suggests an OHU rate of 0.69±0.23 W m^{-2}, consistent with the in-situ estimates of 0.57±0.13, 0.60±0.13, 0.66±0.13 and 0.59±0.13 W m^{-2} from Cheng, Levitus, Ishii and Bagnell, respectively (Figs. 1d and S6d). Different choices of SST dataset and excess temperature estimate (MM C) result in ±0.20 W m^{-2} spread in the GF OHU rate, while uncertainties in the GF kernel lead to ±0.11 W m^{-2} spread (Fig. 1d). Note that the GF OHC uncertainty is no smaller during the Argo era than in earlier periods (Fig. 1c grey shading). This is because the GF method uses the full SST history to infer OHC change (Eq. 1), i.e. the OHU rate at any time is affected by SSTs at all previous times, including their uncertainties. During the Argo era, the Zanna OHU rate sits near the lower limit of our estimate (Fig. 1d); this difference is mostly due to our use of excess temperature for the boundary condition (Fig. S8). The Gebbie estimate is excluded for this comparison because it is not available after 2015.

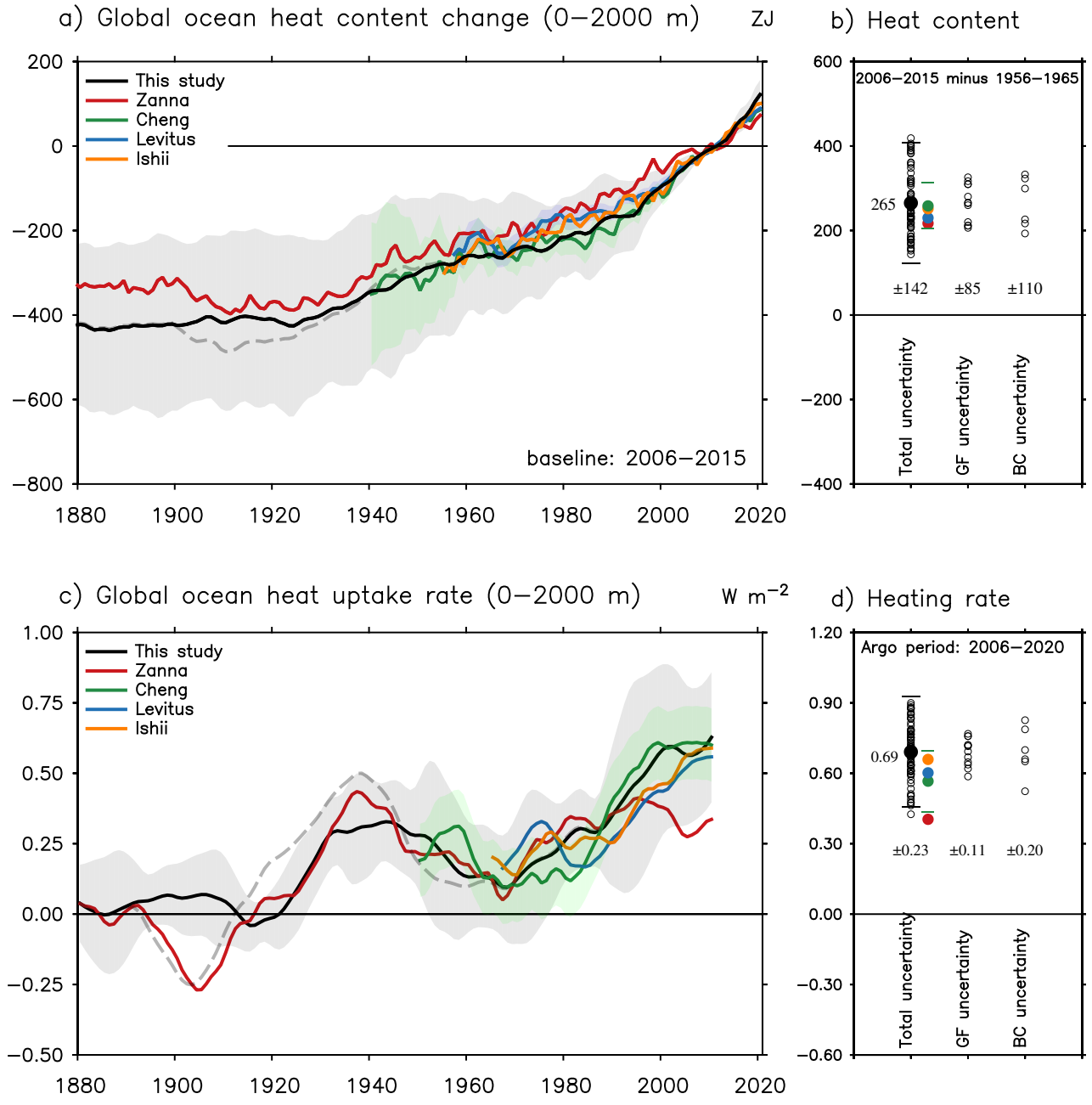

Fig. 1. Global ocean heat uptake during the historical period (0–2000 m). Different estimates are color coded. "This study" and "Zanna" are based on the Green's function (GF) method; the other three are in-situ estimates. a) time evolution of ocean heat content change relative to the 2006-2015 baseline (1 ZJ = 10^{21} J). b) ocean heat content change between 2006–2015 and 1956–1965. c) time evolution of ocean heat uptake rate per unit area of Earth's surface. d) ocean heat uptake rate during the Argo period (2006–2020). In (c), the rate of change is computed as linear trends of a 20-year running window. In (b) and (d), the spread of our GF estimate is decomposed into that due to the GF kernel G and that due to the boundary condition Θ_c^s; individual members are shown as circles. Shading and error bars indicate the 2σ-error. In (a) and (c), the dashed black line is the same as the solid black line, except that it is computed from SST datasets without bias corrections.

Global Energy Budget

In this section, we analyse the global energy budget since 1880 using our GF OHU reconstruction. Methods for deriving the energy budget terms and associated uncertainties are summarised in Table 2. All the energy budget terms are shown as anomalies with respect to the 1870–1880 time mean.

Observation-Based Data. We derive Earth's energy imbalance N from our GF OHU reconstruction, because heating rates in other Earth system components are poorly known prior to 1960. We do not use the GF estimate for OHU below 2000 m because the GF kernel is poorly constrained by observations at those depths (SI Appendix 1C). We obtain the full-depth OHU rate by combining: (i) the GF OHU rate for 0–2000 m depth with (ii) 0.07±0.04 W m^{-2} from Johnson et al. (42) for below 2000 m; the latter only applies to the 1980–2020 period. Earth's heat inventory in recent decades (e.g. 1971–2020) suggests that OHU accounts for 90±6% of N (2, 4, 8). We therefore divide the full-depth OHU rate by 90±6% to derive N. Note that, due to insufficient observations, we assume that: 1) OHU below 2000 m is negligible before 1980 and 2) the fraction of N stored in the ocean is constant in time. These assumptions should be revisited in the future when extended records of Earth's heat inventory become available.

We derive the radiative forcing F and the radiative response R using methods that are independent of the global energy budget, that is $N = F + R$ is not guaranteed by construction. F is obtained from the assessed range in the IPCC sixth assessment report (AR6) (2), which combines lines of evidence from models and observations. R is computed by two methods. The first method (R_{simple}) considers R due to the global-mean surface warming T and a constant climate feedback parameter α (i.e. $R_{\text{simple}} = \alpha T$). The mean and 2σ of T are derived from the HadCRUT5 dataset (43) using its 200 ensemble members. The feedback parameter $\alpha = -1.16 \pm 0.79$ W m^{-2} K^{-1} is obtained from the assessed range in the IPCC AR6 (2). The uncertainty of R_{simple} comes from propagation of error. The second method (R_{spatial}) considers R due to spatially-varying SST and sea ice changes in observations using 3D atmosphere general circulation models. The Cloud Feedback Model Intercomparison project (44) specifically designed an experiment (`amip-piForcing`) to diagnose R_{spatial}; we use the results of eight atmosphere models to compute the mean and 2σ of R_{spatial} (MM E).

The energy imbalance N is derived from the 20-year running window used to compute the OHU rate. For consistency, the radiative forcing F and radiative response R are smoothed by a 20-year running mean. Note that this makes dips in F after volcanic eruptions less obvious.

Budget Closure. Our estimate of Earth's energy imbalance N (Fig. 2a blue line) agrees with the sum of the TOA radiative forcing F and radiative response R within uncertainties all the time since 1880, indicating a closure of the global energy budget. This conclusion is robust regardless of (i) the choice of the R estimate (Fig. 2a black and gray line) and (ii) whether OHU is derived from SST with bias corrections (compare Figs. 2a with S9a). We also use the Zanna and Gebbie OHC estimate to derive N estimates following the method described above. The resulting N estimates agree with $F+R$ during 1880–2020 when considering uncertainties estimated in this study (Fig. S10).

Central Estimate. We compare N against $F+R$ for the central estimate. Our estimate of N closely follows $F + R_{\text{spatial}}$ (Fig. 2a blue and black line); both feature a weak positive trend before 1950 and a stronger one after 1980. The root-mean-squared error between them is 0.14 W m^{-2} over 1880–2014. In comparison, the Zanna and Gebbie N estimates do not track $F+R_{\text{spatial}}$ as closely as our estimate does; both of them suggest a strong decadal variability in N during 1900–1960, which is not seen in $F + R_{\text{spatial}}$ (Fig. S10). The root-mean-squared error between N and $F + R_{\text{spatial}}$ is 0.17 and 0.28 W m^{-2} for the Zanna and Gebbie estimates, respectively.

Our estimate of N (Fig. 2a blue line) agrees better with $F+R_{\text{spatial}}$ (black line) than with $F+R_{\text{simple}}$ (grey line), wherein R_{simple} and R_{spatial} are derived from $R = \alpha T$ and atmosphere models, respectively. This suggests that atmosphere models provide a more realistic estimate of R than the simple model with a constant α. Recent studies have shown that surface warming at different locations affects R differently (45, 46); this mechanism is resolved in R_{spatial}, but not in R_{simple}.

Distinct Phases. We find two distinct phases in the global energy budget. Before 1980, the evolution of Earth's energy imbalance N (Fig. 2b blue line) closely followed that of the radiative forcing F (orange line); the two are not significantly different, considering their uncertainties. Deriving N from SST datasets without bias corrections does not alter this finding (compare Figs. 2b with S9b). After 1980, however, the energy imbalance N started to increase at a slower rate than the radiative forcing F, and the two became significantly different in 2010 (Fig. 2b). N/F measures the fraction of the forcing that went into heating the Earth. The N/F ratio is close to unity before 1980, but gradually decreases after that, reaching 38±15% in 2010 (Table 2). Note that N/F is highly uncertain before 1980 because F is not significantly different from zero during that time.

Reduced Historical Forcing Uncertainty. We infer the radiative forcing F as the difference between N and R following previous studies (7, 47), and compare the result against the F estimate in the IPCC AR6. The uncertainty of the inferred F is derived via propagation of error.

We focus on the 1960–1980 period, for which the F in the IPCC AR6 has a large uncertainty (0.08±0.71 W m^{-2}). The inferred F range is 0.38±0.29 W m^{-2} from $N - R_{\text{simple}}$ and 0.17±0.29 W m^{-2} from $N - R_{\text{spatial}}$. In both cases, the lower bound of the inferred F is substantially less negative than the IPCC AR6 estimate, and the range is about 60% narrower. This uncertainty reduction is comparable to that found by Andrews and Forster (47), who consider the 2005–2015 period. The inferred F also has a smaller uncertainty than the F of IPCC AR6 in 1920–1940 and 2000–2020 (Table 2), but the improvement is less pronounced than in 1960–1980.

Pre-1880 Period. Our global energy budget analysis assumes that Earth's climate is near equilibrium in 1870–1880, consistent with the IPCC AR6 (48). However, some studies argue that an earlier baseline should be used because CO_2 concentration increases started before 1870 (49). As a sensitivity test, we evaluate the global energy budget for

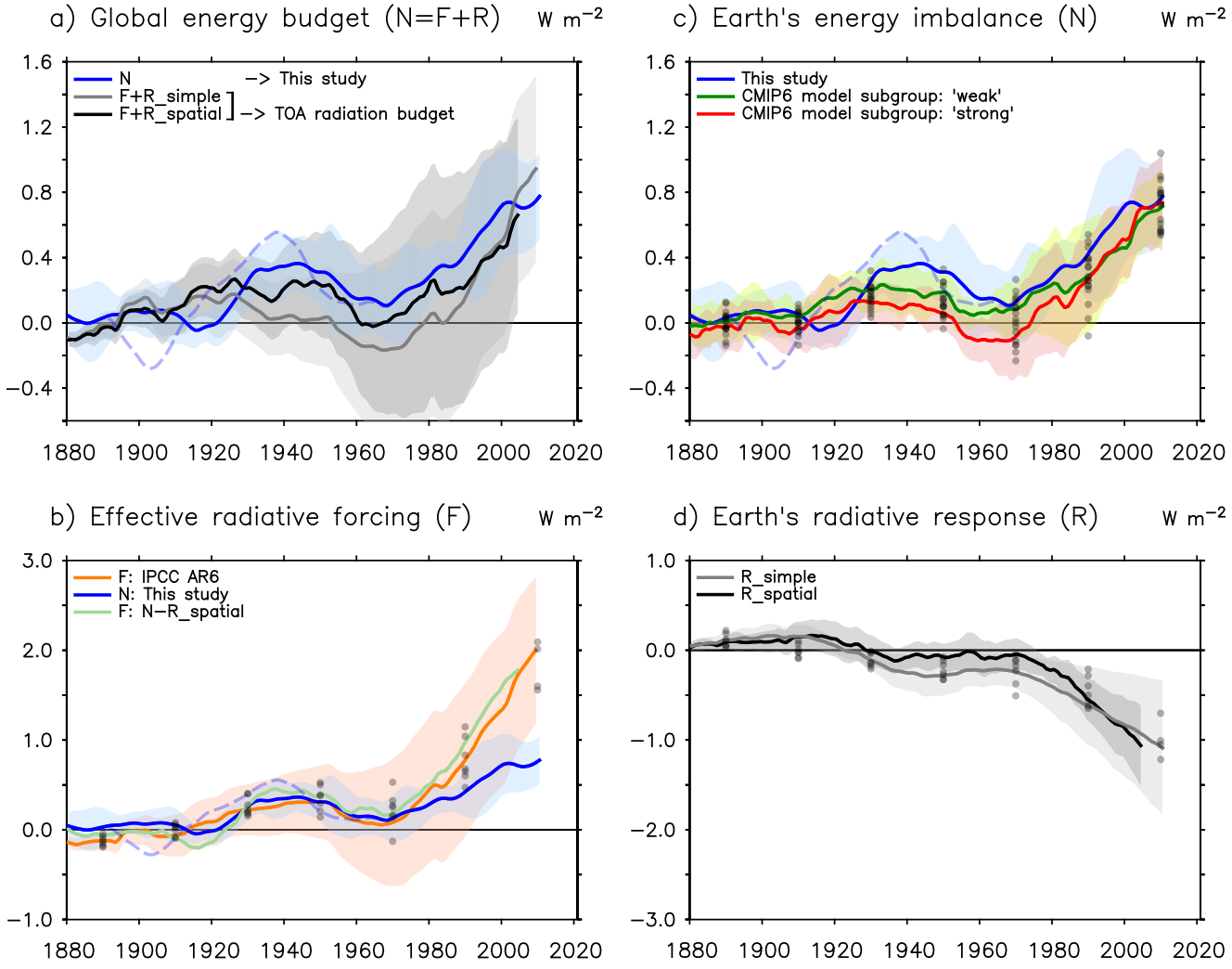

Fig. 2. Evaluating the global energy budget since 1880 using observation-based data. The three components examined here are: Earth's energy imbalance N, the radiative forcing F, and Earth's radiative response R. Methods for deriving N, F and R are summarised in Table 2. In all panels, shading indicates the 2σ-error. F and R are both smoothed by a 20-year running mean. The N estimate of this study is shown as the blue line in (a-c), the same in each panel. The N estimate in the dashed blue line is the same as that in the solid blue line, except that it is computed from SST datasets without bias corrections. In (b-d), simulations from climate models are shown as pale dots, plotted every 20 years for clarity; different panels contain different numbers of model results due to data availability. In (c), the models are split into those with a "weak" and "strong" response to anthropogenic aerosol forcing, respectively.

1700–1880 using surface temperature change reconstructed from palaeoclimate records (MM D). The result shows that Earth's energy imbalance N is dominated by responses to volcanic eruptions in 1700–1800, without a clear sign of long-term increase (Fig. S11). In 1860–1880, the energy imbalance N is close to zero, consistent with our choice of the reference period, i.e. 1870–1880.

Evaluating Climate Model Simulations

In this section, we evaluate the radiative forcing F, the radiative response R and the energy imbalance N simulated in 17 climate models (i.e. atmosphere–ocean general circulation models) participating in the Coupled Model Intercomparison Project Phase 6 (CMIP6) (50) against the observation-based estimates described in the previous section. The energy imbalance N is available for all 17 models up to 2020, while the radiative forcing F and radiative response R are available for 7 models only (up to 2014 in 3 models and 2020 in 4) because they are low priority outputs. We focus on the 1920–1940 and 2000–2020 periods, which sample distinct phases in the observed energy budget. Model results are shown as pale dots in Figs. 2b-d and individually in Figs. S12-15. Methods for deriving the global energy budget from climate models are described in MM E and summarised in Tables 2 and 3. All model results are smoothed by a 20-year running mean to be consistent with the observation-based estimates.

The CMIP6 simulations of F, R and N agree with the observation-based estimates within the 2σ inter-model spread (Figs. 2b-d and Table 2). Notably, CMIP6 models tend to simulate a more negative R than R_{spatial} in 1920–1940 (-0.10 vs. 0.00 W m^{-2}) and a less positive F than the F of IPCC AR6 in 2000–2020 (1.71 vs. 2.02 W m^{-2}) (Table 2).

We next compare the CMIP6 simulations of F, R and N in individual models against the observation-based estimates.

Table 2. Radiative forcing F, radiative response R and Earth's energy imbalance N from observation-based estimates and climate model simulations. The rate of ocean heat uptake is denoted as "dOHU/dt". All quantities are in units of W m^{-2} of Earth's surface area. The 1920–1940 and 2000–2020 averages are selected to demonstrate two distinct phases in the global energy budget. The two R estimates, R_{simple} and R_{spatial}, are both computed from observed surface warming; the difference is that R_{simple} only considers the global-mean warming, whereas R_{spatial} considers the spatially-varying warming using 3D atmosphere models. For climate model simulations, the data source shows the experiment name, with the ensemble size denoted in parentheses. The 2σ-error is derived from various sources/approaches for observation-based estimates, but it is always computed from the inter-model spread for climate model simulations. Different climate model experiments are contrasted in Table 3.

Observation-based estimates				
Variable	1920–1940	2000–2020	Data source	Uncertainty
dOHU/dt 0–2000 m	0.25±0.13	0.63±0.23	GF method	perturbation of inputs
dOHU/dt >2000 m	negligible	0.07±0.04	Johnson et al. (42)	Johnson et al. (42)
dOHU/dt full depth	0.25±0.14	0.70±0.23	sum of previous two	propagation of error
Imbalance N	0.28±0.16	0.78±0.27	dOHU/dt÷(0.90±0.06)	propagation of error
Forcing F	0.23±0.28	2.02±0.82	Forster et al. (2)	Forster et al. (2)
Response R_{simple}	-0.11±0.11	-1.07±0.74	simple model $R = \alpha T$	propagation of error
Response R_{spatial}	0.00±0.17	-1.15±0.51	atmosphere models	inter-model spread
$N \div F$	1.22±1.28	0.38±0.15	N and F	propagation of error
Inferred N	0.23±0.20	0.87±0.58	$F + R_{\text{spatial}}$	propagation of error
Inferred F	0.28±0.21	1.93±0.54	$N - R_{\text{spatial}}$	propagation of error
Inferred R	0.05±0.24	-1.25±0.71	$N - F$	propagation of error
Climate model simulations				
Variable	1920–1940	2000–2020	Data source	CMIP6 variable
dOHU/dt full depth	0.15±0.14	0.71±0.29	`historical` (17)	hfds
Imbalance N	0.16±0.15	0.72±0.28	`historical` (17)	rsdt, rsut, rlut
Forcing F	0.26±0.19	1.71±0.54	`piClim-histall` (7)	rsdt, rsut, rlut
Response R	-0.10±0.15	-0.98±0.45	N and F (7)	N/A
$N \div F$	0.61±0.58	0.43±0.17	N and F (7)	N/A

For a given model, uncertainties of F, R and N are obtained as the standard deviation of the TOA radiative flux in its pre-industrial simulation, after applying the 20-year running mean. This accounts for the fact that model simulations may differ from observations because their unforced variability are in different phases.

For the energy imbalance N, we spilt the 17 models into those with a "weak" response to anthropogenic aerosol forcing (9 models), and those with a "strong" one (8 models) (MM E); their respective multi-model means are shown as the green and red line in Fig. 2c. Eight of the nine "weak" models simulate N that agrees with the observed N (within the 2σ-range) over 90% of the time in 1880–2010 (Fig. S12), but only two of the eight "strong" models do so (Fig. S13). The agreement between the observation-based and simulated N is worse when the former is computed from SST datasets without bias corrections (Fig. 2c compare the blue solid and dashed line).

The radiative forcing F and radiative response R are available for 7 of the 17 climate models. Here we use the inferred F ($N - R_{\text{spatial}}$) and R_{spatial} as the observation-based F and R, respectively. Six of the seven models simulate F that agrees with the observation about 90% of the time in 1880–2004 (Fig. S14), while only two do so for R (Fig. S15). Four of the seven models are the "weak" models, while the rest are the "strong" models. The "weak" models have a more positive F and a more negative R than the "strong" models in the model mean (Fig. S16).

Regional Ocean Heat Uptake

The GF OHC estimate, by construction, only accounts for the OHC change originating from the surface (16, 23); we refer to this as the "excess" OHC change. The difference between the observed total OHC change and the excess OHC change gives the "redistributed" OHC change, which integrates to zero over the global ocean volume (51, 52). In this section, we examine the excess and redistributed contributions to the observed total OHC change at different latitudes. We focus on the zonal-and-depth integrated change over 0–2000 m; a change is computed as the linear trend over 1980–2020, when greenhouse gas forcing dominates. The observed total OHC change is derived from the average of three in-situ datasets: Cheng, Levitus and Ishii.

Latitudinal Distribution. The excess OHC change of this study (i.e. the GF OHC change) has two peaks in both the Indo-Pacific and the Atlantic, located at around 40°S and 30°N (Figs. 3a and b, black line). For the central estimate, the excess OHC change at high latitudes is about twice as large

as that at low latitudes. We compare our estimate with the Bronselaer et al. estimate (52) for excess OHC change (Figs. 3a and b, purple line); the latter is inferred from observed anthropogenic carbon change. The two estimates agree with each other broadly; both of them suggest a greater excess OHC change in the Southern Ocean than the Zanna estimate (16) (Figs. 3a and b, red line). We infer the OHC redistribution as the observed total OHC change minus the excess OHC change. The result suggests that OHC redistribution exhibits alternating positive and negative changes across latitudes (Figs. 3c and d), consistent with previous studies (16, 52, 53).

Regional Integral. We examine the role of OHC redistribution in shaping the observed total OHC change for the North Atlantic integral (30°N–90°N) and the Southern Ocean integral (90°S–30°S). In 1980–2020, the observed global OHC change is about 7.1 ZJ per year, equivalent to 0.45 W m^{-2} over the Earth's surface. The North Atlantic accounts for about 8% of the global change, while the Southern Ocean account for 40%.

In the North Atlantic (Fig. 3b), the excess change of this study (1.5 ZJ yr^{-1}), Bronselaer et al. (52) (0.9 ZJ yr^{-1}) and Zanna et al. (16) (1.1 ZJ yr^{-1}) all exceed the observed total change (0.6 ZJ yr^{-1}) for the central estimate; the ratio of excess to total is 2.5, 1.5 and 1.8, respectively. This implies a net southward heat redistribution, or a weakening of the northward heat transport, across 30°N. Note that our estimate of excess change is highly uncertain in the North Atlantic (Fig. 3b), which prevents an accurate estimate of the redistributed change there.

In the Southern Ocean (Figs. 3a and b), the excess change of this study and Bronselaer et al. (52) are about the same as the observed total change, especially in the Indo-Pacific sector (Fig. 3a, numbers). This indicates that the redistributed change is close to zero when aggregated over the Southern Ocean, despite its marked patterns there, in contrast with the North Atlantic case.

Summary and Discussion

Earth's energy imbalance N, the radiative forcing F and the radiative response R are essential quantities for monitoring the trajectory of anthropogenic climate change; they are linked through the global energy budget $N = F + R$. The ocean volume-integrated warming dominates Earth's energy imbalance N on multiannual timescales. Poor observational sampling prevents an estimate of global ocean warming before 1960, which leaves a gap in the global energy budget record.

In this study, we produce a reconstruction of global ocean heat uptake beginning in 1880 via a Green's function approach that relies on surface observations, hence alleviating the sampling issue in early periods. Our estimate of ocean warming is consistent with those derived from in-situ temperature profiles since 1960. From our estimate we obtain a timeseries of Earth's energy imbalance N, i.e. the net global-mean top-of-atmosphere (TOA) radiative flux, since 1880.

We highlight two findings in this study. First, our estimate of Earth's energy imbalance N is consistent with the current best estimates of radiative forcing F (2) and radiative response R (R_{spatial}) during 1880–2020. In particular, our N estimate reduces the discrepancy between $F+R$ and N during 1900–1960 in previous studies (Fig. S10), improving the understanding of historical climate change in early periods.

Second, our analysis reveals two distinct phases in the global energy budget. In 1880–1980, Earth's energy imbalance N closely followed the radiative forcing F. After 1980, however, the imbalance N increased at a slower rate than the forcing F; N only amounts to 38±15% of F in 2000–2020. While the causes of those distinct phases are unclear, this finding is consistent with recent studies showing that the climate feedback parameter α has been more negative (stable) since 1980 than it was in the preceding decades (45, 46). That is, Earth's radiative response R per unit global warming is increasing, which promotes a more negative R, hence a lower N/F ratio. The change in α is linked to the change in SST warming pattern; the recent La-Nina-like pattern makes α more negative because it increases low cloud cover (54).

A major consequence of OHU is sea-level rise through ocean thermal expansion. The ocean thermal expansion derived from the GF OHC estimate (this study) agrees with that derived from the total sea-level rise minus ocean-mass change, considering uncertainties (Fig. S17a, MM F). This indicates that the GF OHC estimate is consistent with the sea-level budget. Nonetheless, we note there are marked differences in the central estimates of thermal expansion derived from the above two approaches (Fig. S17a). This hinders a tight constraint on OHC change from the sea-level budget in the early 20th century.

Any systematic error in SST datasets will result in systematic errors in our estimate of Earth's energy imbalance N, because SST errors are propagated to N via the Green's function. Past studies suggest that the cold excursion in 1900–1920 and the World War 2 warm anomaly in 1939–1945 may be artefacts of the SST datasets, due to poor sampling coverage and inhomogeneity of instrumentation (24–28). We find that removing those two features produces a N estimate that agrees better with: 1) the observation-based TOA radiation budget ($F + R$) and 2) the historical simulation of N in climate models.

Materials and Methods

A. Excess Heat and Green's Function. Excess heat is the additional heat entering the ocean from the surface. The governing equation of excess heat, written in terms of excess temperature Θ_{e}, is given by:

$$(\frac{\partial}{\partial t} + L)\Theta_{\mathrm{e}}(\mathbf{r}, t) = Q_{\mathrm{a}}(\mathbf{r}, t), \qquad [2]$$
$$\text{Initial condition: } \Theta_{\mathrm{e}}(\mathbf{r}, 0) = 0,$$

where t is time and $\mathbf{r}$ a 3D position vector in the ocean. Q_{a} is the surface heat flux anomaly relative to the climatology. L is the 3D ocean transport operator, which evolves an ocean tracer field forward in time; it encodes the net effect of ocean transport, from large-scale advection to small-scale mixing. Multiplying Θ_{e} with the specific heat and density of seawater gives excess heat. Integrating excess heat over the global ocean volume gives global ocean heat content (OHC) change. Diagnostics similar to Θ_{e} have been used in the literature, for instance, the fixed-circulation temperature change in Winton et al. (55), the added temperature in Gregory et al. (51) and the material warming in Zika et al. (53).

The Green's function (GF) approach solves Θ_{e} in Eq. 2 by propagating its boundary condition $\Theta_{\mathrm{e}}^{\mathrm{s}}$. The propagation is done via the boundary GF G, which encodes the ocean's surface-to-interior transport (advection+mixing). The above process can be

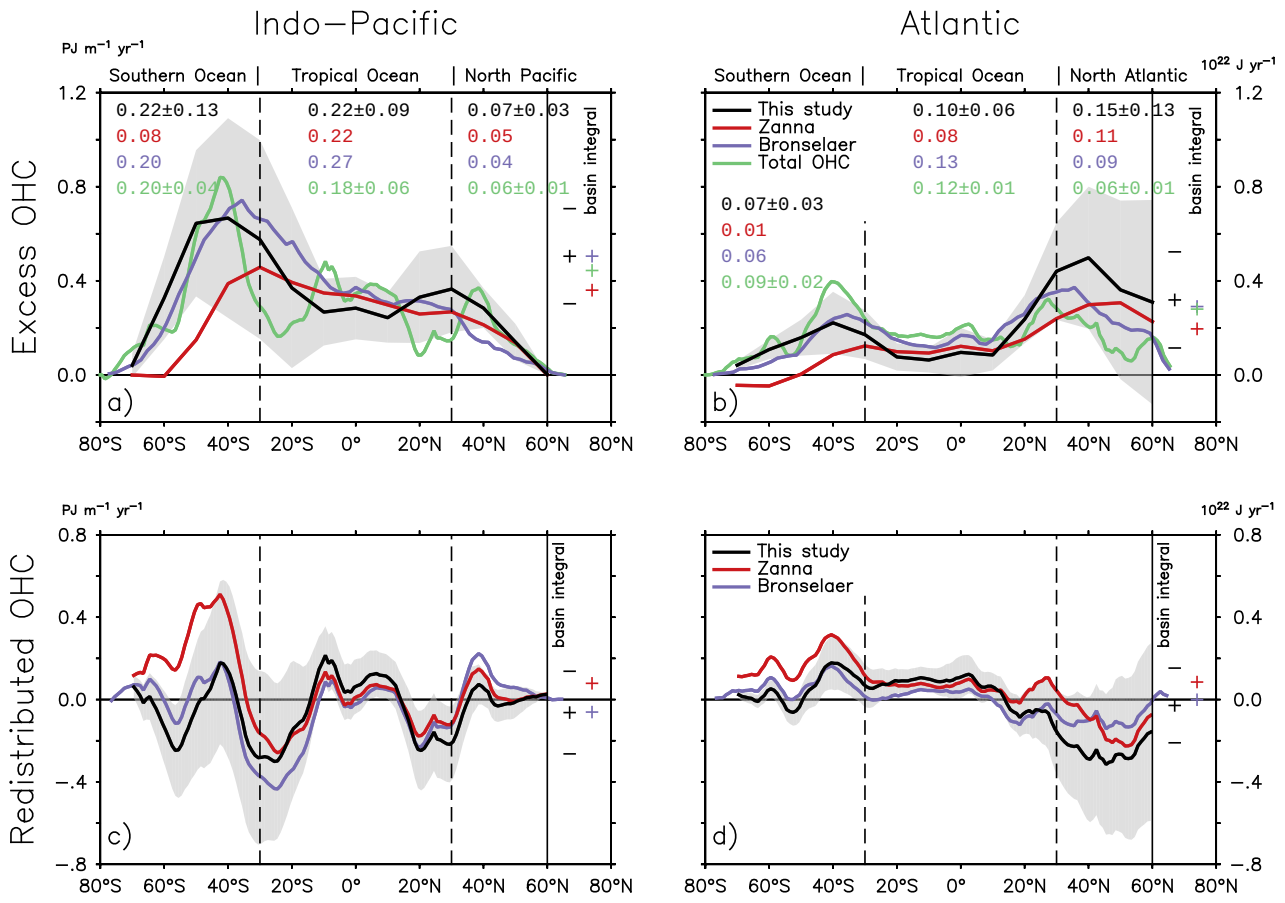

Fig. 3. Excess and redistributed OHC change integrated zonally and vertically (0–2000 m) for ocean basins. The change is computed as the linear trend over 1980–2020, and refers to the left-hand axis. The excess OHC change is from: this study (black), Zanna et al. (16) (red) and Bronselaer et al. (52) (purple). The observed total OHC change (green) is included for comparison. The redistributed OHC change is computed as the difference between the observed total and excess change. The basin-integrated change is shown by the "+" sign in the rightmost portion of each panel, referring to the right-hand axis. The numbers show the changes integrated over three latitude bands, separated by vertical dashed lines, in units of 10^{22} J yr^{-1}. The colors of the numbers and the plus signs match those of the lines, indicated in the legends. Shading, horizontal bar and the "±" sign indicate the 2σ-range.

written as the following sum over space and time:

$$\Theta_{\rm e}(\mathbf{r},t) = \int_{\Omega} \mathrm{d}^2\mathbf{r}_{\rm s} \int_{-\infty}^{t} G(\mathbf{r}_{\rm s}, t-t_{\rm s} \mid \mathbf{r}) \Theta_{\rm e}^{\rm s}(\mathbf{r}_{\rm s}, t_{\rm s})\, \mathrm{d}t_{\rm s}, \qquad [3]$$

where Ω denotes the global ocean surface and $(\mathbf{r}_{\rm s}, t_{\rm s})$ are coordinate variables for surface quantities. Note that Eq. 3 is a generalisation of Eq. 1.

The GF approach is useful because it can provide an OHC estimate without subsurface temperature measurements; it only requires surface temperature as input, given that the GF G is known. For this reason, the GF approach has been used to reconstruct OHC in the past 2000 years (56). The GF approach, however, has a number of limitations. First, the GF is assumed to be stationary in time, ignoring potential changes in ocean transports due to changes in climate states. Second, estimating the GF from observations is a highly underdetermined problem as there are many more unknowns than tracer constraints, a challenge compounded by poor sampling of ocean transient tracers in space and time. Lastly, the boundary condition $\Theta_{\rm e}^{\rm s}$ is not observable and must be partly inferred from model simulations.

B. Observational Green's Functions. To infer the GF G from observations, we first rewrite Eq. 3 into a general form

$$X(\mathbf{r},t) = \int_{\Omega} \mathrm{d}^2\mathbf{r}_{\rm s} \int_{-\infty}^{t} G(\mathbf{r}_{\rm s}, t-t_{\rm s} \mid \mathbf{r}) X^{\rm s}(\mathbf{r}_{\rm s}, t_{\rm s})\, \mathrm{d}t_{\rm s}, \qquad [4]$$

where X is the concentration of a given tracer; e.g. $\Theta_{\rm e}$ or CFC-11. $X^{\rm s}$ is X at the surface. Eq. 4 holds because all tracers in the ocean experience the same ocean transports (i.e. velocities and diffusivities) (17). Each tracer observation, i.e. $X(\mathbf{r},t)$, forms a constraint on G at $\mathbf{r}$ via Eq. 4. Here $\mathbf{r}$ and t are the location and time of observations, respectively. A collection of n observations at $\mathbf{r}$ thus forms n equations for G there. In practice, observations are insufficient constraints of G, because the number of observations is much smaller than the number of unknowns in G. Note that G is a function of ocean surface locations and transit times. We solve this underdetermined problem using the Maximum Entropy method (18, 20). Among infinitely many G solutions that satisfy observations, the Maximum Entropy method chooses the one that is the most "similar" to a prior estimate of G (measured by their "relative entropy"). This procedure can be cast into a constrained optimisation problem and solved using standard numerical routines.

Details on formulating and solving the Maximum Entropy problem are documented in Wu and Gregory (23) and summarised in Fig. S1. We use four observations of tracers to infer G at every $\mathbf{r}$; they are CFC-11 and CFC-12 in the GLODAP data (57) (observed at 1994) and the climatological temperature and salinity. We combine these tracers together because their distributions are primarily controlled by the climatological ocean transport. Treatment of the observations is described in SI Appendix 1. We generate four realisations of the GLODAP data by randomly perturbing the central estimate with the standard error of the data. We use G computed from two climate models and an ocean state estimate as first-guess solutions for inferring G from observations. The climate models are HadCM3 (1.25°×1.25°) (58) and FAMOUS (3.75°×2.50°) (59). The state estimate is ECCO-GODAE (1°×1°) (29). The 4 sets of observational constraints and 3 first-guess solutions result in 12 sets of observational GFs.

A lack of diversity in the first-guess solution of G is a limitation of this study. We only use three first-guess solutions here because computing G requires carrying out customised ocean tracer simulations, which have not been done in other models.

None of our first-guess solutions is derived from eddy-resolving models. In all of them, horizontal eddy mixing of tracers is parameterised using the Redi (60) and Gent and McWilliams (61) schemes. Errors in eddy parameterisation affect our results by affecting the first-guess solutions. Although observational constraints would correct some of the errors, it is unclear how much still remains. In future studies, deriving G with different eddy parameterisation schemes and model resolutions would help to address this question.

The GF OHC estimate and the Cheng OHC estimate (31) are not fully independent, because HadCM3 is used in both, although in different ways. To test the impact of this dependency, we have re-computed the GF OHC estimate using the first guess from FAMOUS and ECCO-GODAE, i.e. removing the HadCM3 information. This results in little change in our OHC estimate.

C. Ocean Heat Uptake Boundary Conditions. We refer $\Theta_{\rm e}^{\rm s}$ as "sea surface excess temperature" (SSTe) to correspond with "sea surface temperature anomaly" (SSTa) used in Zanna et al. (16). The main difference between SSTa and SSTe is that the latter does not contain ocean temperature redistribution (51). Keeping redistributed temperature in the boundary condition may bias the GF OHC estimate. This is because the GF method only accounts for tracers originating from the surface, but redistributed temperature has sources/sinks throughout water columns (23).

We estimate SSTe by combining three SSTa datasets from observations with two SSTe simulations from climate models (SI Appendix 2, summarised in Fig. S3). Specifically, we replace the global mean of SSTe from climate models with the global mean of SSTa from observations. That is, we only use the spatial anomalies (relative to global mean) from model simulations, not their global means. Note that we omit the difference between SSTe and SSTa in the global mean. A model simulation suggests that SSTe is about 0.1 K warmer than SSTa in the global mean after 1960 (23), probably due to reduced ocean convection. This suggests that our SSTe boundary condition may contain a cold bias in recent decades. Both SSTa and SSTe are expressed as anomalies relative to the 1870–1880 time mean, assuming that the ocean is near equilibrium during that period. Our result is not sensitive to small changes in the baseline. For instance, adding a constant offset of 0.1 K to SSTe, as suggested by Jarvis and Forster (62), only increases our estimate of Earth's energy imbalance N by ∼0.01 W m^{-2} after 1930 (Fig. S18).

We process the global mean of SSTa in two steps. The first step applies a low-pass filter to reduce the impact from interannual heat redistribution. The second step removes two potential biases in SST datasets before 1960 (shown in Fig. S5), which are discussed in the main text. See SI Appendix 2 for further information of the two-step processing.

The SSTe used here is physically connected to the SSTa used in MM E to derive Earth's radiative response $R_{\rm spatial}$. Specifically, SSTe is the part of SSTa that originates from surface heat flux change $Q_{\rm a}$ (23). We enforce this relationship by first identifying climate models that well reproduce the observed SSTa trends, and then using their $Q_{\rm a}$ fields to carry out SSTe simulations following Eq. 2 (SI Appendix 2).

D. Global Energy Budget in 1700–1880 . This supplementary analysis uses the same method as the main analysis for 1880–2022. Because temperature datasets used in the main analysis are not available before 1850, we replace them with PAGES2k data (63), which is based on palaeoclimate proxies. The PAGES2k temperature is used for computing Earth's radiative response R as well as providing the global mean for the SSTe boundary condition, which is assumed to be globally uniform. PAGES2k data is derived from 7 distinct reconstruction methods, each with 1000 ensemble members. The SSTe boundary condition consists of 7 members, each of which is the ensemble mean of a reconstruction method. This choice is to reduce the cost of evaluating Eq. 3. All 7000 members are used to derive the 2σ-range for computing R. Temperature change is computed with respect to the 1700–1750 baseline.

E. Climate Model Simulations. We use four climate model experiments here. They are the coupled atmosphere–ocean experiment `historical` (1850–2020) with its pre-industrial control `piControl`, and the atmosphere-only experiments `piClim-histall` (1850–2020) and `amip-piForcing` (1870–2014). In all of them, the net TOA radiative flux is computed using TOA incoming shortwave flux (`rsdt`), TOA outgoing shortwave flux (`rsut`) and TOA outgoing longwave flux (`rlut`) from CMIP6 standard outputs. The ocean heat uptake (OHU) rate in the `historical` experiment is derived from the net downward heat flux at the sea surface (`hfds`). Note that climate models tend to store a greater fraction of the TOA imbalance in the ocean compare to observations (96% vs. 90%) because their deficiencies in simulating melting of terrestrial ice and

warming of solid Earth (64). The standard `historical` experiment stops at 2014; we extend it to 2020 using its `SSP2-4.5` (medium emission) extension. The distinguishing features of the experiments and our uses of them are summarised in Table 3.

E.1. Global Energy Budget Terms. The global energy budget terms of historical simulations are derived from the `historical` and `piClim-histall` experiments. Earth's energy imbalance N is derived from the net TOA flux in the `historical` experiment. The contributions of radiative forcing F and radiative response R to the energy imbalance N cannot be separated in the `historical` experiment. We diagnose F using the `piClim-histall` experiment (65), which is a parallel experiment to `historical`. The `piClim-histall`, by construction, has the same F as in `historical`, but zero R, because its SST and sea ice are fixed to the pre-industrial condition. We derive R of the `historical` experiment as the difference $R = N - F$. We use the `historical` experiment from 17 models, which are listed in Table S1; seven of them have the `piClim-histall` experiment: CNRM-CM6-1, GISS-E2-1-G, IPSL-CM6A-LR, MIROC6, CanESM5, HadGEM3-GC31-LL, and NorESM2-LM.

The `amip-piForcing` experiment provides an estimate of the radiative response R due to observed SST and sea ice changes, which are prescribed as time-varying boundary conditions, with constant pre-industrial forcing (44, 46). We use the `amip-piForcing` experiment from eight models: CanESM5, CESM2, CNRM-CM6-1, HadGEM3-GC31-LL, IPSL-CM6A-LR, MIROC6, MRI-ESM2-0, and TaiESM1. Note that the `historical` and `amip-piForcing` experiment with a given model produce different R because their SST and sea ice fields are different.

E.2. Model Drifts and Energy Leakage. Climate model simulations often contain "climate drift" (unforced trends) (66) and non-closure of the energy budget (67, 68), which are collectively referred to as climate drift here. In practice, the climate drift can be estimated from the steady-state simulation, and then removed from the climate change simulation of interest, assuming the same drift to be present in both simulations (66–68).

For the coupled simulation `historical`, we remove the climate drift by removing its parallel steady-state simulation `piControl`. The de-drifting substantially improves the energy conservation in climate models. To demonstrate this we compare the TOA radiative flux and the OHU rate (both are global means). Before de-drifting, the TOA radiative flux is much larger than the OHU rate in several models (Fig. S19), suggesting a non-conservation of energy. After de-drifting, the TOA radiative flux closely matches the OHU rate in all 17 models examined here (Fig. S20), implying that the energy leakage is of similar size between the `historical` and `piControl` simulation. For `piClim-histall` and `amip-piForcing`, we remove the climate drift by removing their 1870–1880 time mean, because they have no parallel steady-state simulations. The late 19th-century is a common choice for defining the steady state climate; e.g. it is used to design the `piControl` experiment. The 1870–1880 is also used as the steady-state reference for estimating OHU in this study (Table 1).

E.3. "Strong" and "Weak" Models. We classify each of the 17 climate models as having a "strong" or a "weak" response to anthropogenic aerosol forcing (Table S1). We classify a model as "strong" if its net surface heat loss relative to the pre-industrial control is stronger than 2 W m^{-2}, averaged over the North Atlantic (30°N–65°N) and 1950–1980, when the aerosol forcing dominates. This gives a similar classification of models as in Robson et al. (69).

F. Sea Level Budget. The global-mean sea-level rise can be decomposed into contributions from a) ocean-mass change and b) ocean thermal expansion. Those are termed as the barystatic and thermosteric component, respectively (70). We derive the global-mean sea level and its barystatic component from observation-based reconstructions in Frederikse et al. (71), which covers 1900–2018. Specifically, the global-mean sea level is obtained from tide-gauge and satellite-altimetry observations and the barystatic change is estimated from mass change of glaciers, ice sheets and terrestrial water. We convert OHC change (ZJ) to thermosteric change (mm) via the expansion efficiency of heat, 0.11 mm ZJ^{-1}. This number is derived in Zanna et al. (16) based on climatological ocean temperature and salinity in observations.

Data and Software Availability. Ocean heat uptake data of this study is available at https://doi.org/10.5281/zenodo.11107298. CMIP6 data is available at https://esgf-node.llnl.gov. ECCOv4 data can be downloaded from https://www.ecco-group.org. In-situ ocean heat content data are downloaded from: http://www.ocean.iap.ac.cn (Cheng), https://www.data.jma.go.jp (Ishii), and https://www.ncei.noaa.gov (Levitus).

ACKNOWLEDGMENTS. This project was supported by the UK Natural Environment Research Council (NERC) grant NE/P019099/1 for the TICTOC project. We are grateful to colleagues in the TICTOC project for many useful discussions. Q.W. and J.M.G. received support from the European Research Council (ERC) under the European Union's Horizon 2020 research and innovation programme (grant agreement No 786427, project "Couplet"). L.Z. received support from the NSF OCE grant 2048576 and M^{2}LInES through support from Schmidt Sciences, LLC. S.K. received support from the UK NERC grant NE/P019218/1 and NE/W007258/1. We acknowledge the World Climate Research Programme's Working Group on Coupled Modelling, which is responsible for CMIP, for producing and making available their model output. We thank the editor and anonymous reviewers for their useful comments and suggestions.

1. G Myhre, et al., Anthropogenic and natural radiative forcing in *Climate Change 2013: The Physical Science Basis. Contribution of Working Group I to the Fifth Assessment Report of the Intergovernmental Panel on Climate Change*, eds. T Stocker, et al. (Cambridge University Press), p. 659–740 (2013).
2. P Forster, et al., The earth's energy budget, climate feedbacks, and climate sensitivity in *Climate Change 2021: The Physical Science Basis. Contribution of Working Group I to the Sixth Assessment Report of the Intergovernmental Panel on Climate Change*, eds. V Masson-Delmotte, et al. (Cambridge University Press), pp. 923–1054 (2021).
3. P Forster, JM Gregory, The climate sensitivity and its components diagnosed from Earth radiation budget data. *J. Clim.* **19**, 39–52 (2006).
4. K Von Schuckmann, et al., Heat stored in the Earth system 1960–2020: where does the energy go? *Earth Syst. Sci. Data* **15**, 1675–1709 (2023).
5. JM Gregory, RJ Stouffer, SCB Raper, PA Stott, NA Rayner, An observationally based estimate of the climate sensitivity. *J. Clim.* **15**, 3117–3121 (2002).
6. A Otto, et al., Energy budget constraints on climate response. *Nat. Geosci.* **6**, 415–416 (2013).
7. DM Murphy, et al., An observationally based energy balance for the Earth since 1950. *J. Geophys. Res.* **114**, D17107 (2009).
8. J Church, et al., Sea level change in *Climate Change 2013: The Physical Science Basis. Contribution of Working Group I to the Fifth Assessment Report of the Intergovernmental Panel on Climate Change*, eds. T Stocker, et al. (Cambridge University Press), p. 1137–1216 (2013).
9. C Zhou, MD Zelinka, AE Dessler, M Wang, Greater committed warming after accounting for the pattern effect. *Nat. Clim. Chang.* **11**, 132–136 (2021).
10. B Meyssignac, et al., Measuring global ocean heat content to estimate the Earth energy imbalance. *Front. Mar. Sci.* **6**, 432 (2019).
11. NG Loeb, et al., Satellite and ocean data reveal marked increase in Earth's heating rate. *Geophys. Res. Lett.* **48**, e2021GL093047 (2021).
12. T Boyer, et al., Sensitivity of global upper-ocean heat content estimates to mapping methods, XBT bias corrections, and baseline climatologies. *J. Clim.* **29**, 4817–4842 (2016).
13. A Savita, et al., Quantifying spread in spatiotemporal changes of upper-ocean heat content estimates: an internationally coordinated comparison. *J. Clim.* **35**, 851–875 (2022).
14. GC Johnson, et al., Argo—Two Decades: global oceanography, revolutionized. *Annu. Rev. Mar. Sci.* **14**, 379–403 (2022).
15. G Gebbie, P Huybers, The Little Ice Age and 20th-century deep Pacific cooling. *Science* **363**, 70–74 (2019).
16. L Zanna, S Khatiwala, JM Gregory, J Ison, P Heimbach, Global reconstruction of historical ocean heat storage and transport. *Proc. Natl. Acad. Sci.* **116**, 1126–1131 (2019).
17. TW Haine, TM Hall, A generalized transport theory: water-mass composition and age. *J. Phys. Oceanogr.* **32**, 1932–1946 (2002).
18. S Khatiwala, F Primeau, T Hall, Reconstruction of the history of anthropogenic CO2 concentrations in the ocean. *Nature* **462**, 346–349 (2009).
19. S Khatiwala, F Primeau, M Holzer, Ventilation of the deep ocean constrained with tracer observations and implications for radiocarbon estimates of ideal mean age. *Earth Planet. Sci. Lett.* **325-326**, 116–125 (2012).
20. M Holzer, FW Primeau, WM Smethie, S Khatiwala, Where and how long ago was water in the western North Atlantic ventilated? Maximum entropy inversions of bottle data from WOCE line A20. *J. Geophys. Res.* **115**, C07005 (2010).
21. Q Wu, X Zhang, JA Church, J Hu, JM Gregory, Evolving patterns of sterodynamic sea-level rise under mitigation scenarios and insights from linear system theory. *Clim. Dyn.* **57**, 635–656 (2021).
22. M Holzer, T DeVries, W Smethie, The ocean's global ^{39}Ar distribution estimated with an ocean circulation inverse model. *Geophys. Res. Lett.* **46**, 7491–7499 (2019).

Table 3. A comparison of climate model experiments used in this study.

name	configuration	atmospheric composition	SST	TOA net radiative flux is	climate change is anomaly wrt
`piControl`	coupled atmosphere–ocean	pre-industrial	predicted by model	model drift	N/A
`historical` (1850–2014)	coupled atmosphere–ocean	time-varying historical	predicted by model	model `historical` N	parallel `piControl`
`piClim-histall` (1850–2014)	atmosphere-only	time-varying historical	climatology of `piControl`	model `historical` F	its own 1870–1880 time mean
`amip-piForcing` (1870–2014)	atmosphere-only	pre-industrial	observations, time-varying	observation-based R estimate	its own 1870–1880 time mean

23. Q Wu, JM Gregory, Estimating ocean heat uptake using boundary Green's functions: a perfect-model test of the method. *J. Adv. Model. Earth Syst.* **14**, e2022MS002999 (2022).
24. CK Folland, O Boucher, A Colman, DE Parker, Causes of irregularities in trends of global mean surface temperature since the late 19th century. *Sci. Adv.* **4**, eaao5297 (2018).
25. K Cowtan, R Rohde, Z Hausfather, Evaluating biases in sea surface temperature records using coastal weather stations. *Q. J. Royal Meteorol. Soc.* **144**, 670–681 (2018).
26. JJ Kennedy, NA Rayner, CP Atkinson, RE Killick, An ensemble data set of sea surface temperature change from 1850: the Met Office Hadley Centre HadSST.4.0.0.0 data set. *J. Geophys. Res. Atmospheres* **124**, 7719–7763 (2019).
27. D Chan, P Huybers, Correcting observational biases in sea surface temperature observations removes anomalous warmth during World War II. *J. Clim.* **34**, 4585–4602 (2021).
28. S Sippel, et al., Early-twentieth-century cold bias in ocean surface temperature observations. *Nature* **635**, 618–624 (2024).
29. C Wunsch, P Heimbach, Practical global oceanic state estimation. *Phys. D: Nonlinear Phenom.* **230**, 197–208 (2007).
30. G Gebbie, P Huybers, Total Matrix Intercomparison: a method for determining the geometry of water-mass pathways. *J. Phys. Oceanogr.* **40**, 1710–1728 (2010).
31. L Cheng, et al., Improved estimates of ocean heat content from 1960 to 2015. *Sci. Adv.* **3**, e1601545 (2017).
32. S Levitus, et al., World ocean heat content and thermosteric sea level change (0-2000 m), 1955-2010. *Geophys. Res. Lett.* **39** (2012).
33. M Ishii, et al., Accuracy of global upper ocean heat content estimation expected from present observational data sets. *SOLA* **13**, 163–167 (2017).
34. A Bagnell, T DeVries, 20th century cooling of the deep ocean contributed to delayed acceleration of Earth's energy imbalance. *Nat. Commun.* **12**, 4604 (2021).
35. JM Lyman, et al., Robust warming of the global upper ocean. *Nature* **465**, 334–337 (2010).
36. A Minière, K Von Schuckmann, JB Sallée, L Vogt, Robust acceleration of Earth system heating observed over the past six decades. *Sci. Reports* **13**, 22975 (2023).
37. L Cheng, G Foster, Z Hausfather, KE Trenberth, J Abraham, Improved quantification of the rate of ocean warming. *J. Clim.* **35**, 4827–4840 (2022).
38. A Storto, C Yang, Acceleration of the ocean warming from 1961 to 2022 unveiled by large-ensemble reanalyses. *Nat. Commun.* **15**, 545 (2024).
39. Y Li, JA Church, TJ McDougall, PM Barker, Sensitivity of observationally based estimates of ocean heat content and thermal expansion to vertical interpolation schemes. *Geophys. Res. Lett.* **49**, e2022GL101079 (2022).
40. AJ Dittus, et al., Sensitivity of historical climate simulations to uncertain aerosol forcing. *Geophys. Res. Lett.* **47** (2020).
41. S Gulev, et al., Changing state of the climate system in *Climate Change 2021: The Physical Science Basis. Contribution of Working Group I to the Sixth Assessment Report of the Intergovernmental Panel on Climate Change*, eds. V Masson-Delmotte, et al. (Cambridge University Press), pp. 287–422 (2021).
42. GC Johnson, et al., Global oceans. *Bull. Am. Meteorol. Soc.* **104**, S146–S206 (2023).
43. CP Morice, et al., An updated assessment of near-surface temperature change from 1850: the HadCRUT5 data set. *J. Geophys. Res. Atmospheres* **126**, e2019JD032361 (2021).
44. MJ Webb, et al., The Cloud Feedback Model Intercomparison Project (CFMIP) contribution to CMIP6. *Geosci. Model. Dev.* **10**, 359–384 (2017).
45. JM Gregory, T Andrews, P Ceppi, T Mauritsen, MJ Webb, How accurately can the climate sensitivity to CO2 be estimated from historical climate change? *Clim. Dyn.* **54**, 129–157 (2020).
46. T Andrews, et al., On the effect of historical SST patterns on radiative feedback. *J. Geophys. Res. Atmospheres* **127**, e2022JD036675 (2022).
47. T Andrews, PM Forster, Energy budget constraints on historical radiative forcing. *Nat. Clim. Chang.* **10**, 313–316 (2020).
48. D Chen, et al., Framing, context, and methods in *Climate Change 2021: The Physical Science Basis. Contribution of Working Group I to the Sixth Assessment Report of the Intergovernmental Panel on Climate Change*, eds. V Masson-Delmotte, et al. (Cambridge University Press), pp. 147–286 (2021).
49. E Hawkins, et al., Estimating changes in global temperature since the preindustrial period. *Bull. Am. Meteorol. Soc.* **98**, 1841–1856 (2017).
50. V Eyring, et al., Overview of the Coupled Model Intercomparison Project Phase 6 (CMIP6) experimental design and organization. *Geosci. Model. Dev.* **9**, 1937–1958 (2016).
51. JM Gregory, et al., The Flux-Anomaly-Forced Model Intercomparison Project (FAFMIP) contribution to CMIP6: investigation of sea-level and ocean climate change in response to CO2 forcing. *Geosci. Model. Dev.* **9**, 3993–4017 (2016).
52. B Bronselaer, L Zanna, Heat and carbon coupling reveals ocean warming due to circulation changes. *Nature* **584**, 227–233 (2020).
53. JD Zika, JM Gregory, EL McDonagh, A Marzocchi, L Clément, Recent water mass changes reveal mechanisms of ocean warming. *J. Clim.* **34**, 3461–3479 (2021).
54. C Zhou, MD Zelinka, SA Klein, Analyzing the dependence of global cloud feedback on the spatial pattern of sea surface temperature change with a Green's function approach. *J. Adv. Model. Earth Syst.* **9**, 2174–2189 (2017).
55. M Winton, SM Griffies, BL Samuels, JL Sarmiento, TL Frölicher, Connecting changing ocean circulation with changing climate. *J. Clim.* **26**, 2268–2278 (2013).
56. G Gebbie, Combining modern and paleoceanographic perspectives on ocean heat uptake. *Annu. Rev. Mar. Sci.* **13**, 255–281 (2021).
57. RM Key, et al., A global ocean carbon climatology: results from Global Data Analysis Project (GLODAP). *Glob. Biogeochem. Cycles* **18**, GB4031 (2004).
58. C Gordon, et al., The simulation of SST, sea ice extents and ocean heat transports in a version of the Hadley Centre coupled model without flux adjustments. *Clim. Dyn.* **16**, 147–168 (2000).
59. RS Smith, JM Gregory, A Osprey, A description of the FAMOUS (version XDBUA) climate model and control run. *Geosci. Model. Dev.* **1**, 53–68 (2008).
60. MH Redi, Oceanic isopycnal mixing by coordinate rotation. *J. Phys. Oceanogr.* **12**, 1154–1158 (1982).
61. PR Gent, JC Mcwilliams, Isopycnal mixing in ocean circulation models. *J. Phys. Oceanogr.* **20**, 150–155 (1990).
62. A Jarvis, PM Forster, Estimated human-induced warming from a linear temperature and atmospheric CO2 relationship. *Nat. Geosci.* **17**, 1222–1224 (2024).
63. R Neukom, et al., Consistent multidecadal variability in global temperature reconstructions and simulations over the Common Era. *Nat. Geosci.* **12**, 643–649 (2019).
64. FJ Cuesta-Valero, A García-García, H Beltrami, J Finnis, First assessment of the earth heat inventory within CMIP5 historical simulations. *Earth Syst. Dyn.* **12**, 581–600 (2021).
65. R Pincus, PM Forster, B Stevens, The Radiative Forcing Model Intercomparison Project (RFMIP): experimental protocol for CMIP6. *Geosci. Model. Dev.* **9**, 3447–3460 (2016).
66. A Sen Gupta, NC Jourdain, JN Brown, D Monselesan, Climate drift in the CMIP5 models. *J. Clim.* **26**, 8597–8615 (2013).
67. W Hobbs, MD Palmer, D Monselesan, An energy conservation analysis of ocean drift in the CMIP5 global coupled models. *J. Clim.* **29**, 1639–1653 (2016).
68. D Irving, W Hobbs, J Church, J Zika, A mass and energy conservation analysis of drift in the CMIP6 ensemble. *J. Clim.* **34**, 3157–3170 (2020).
69. J Robson, et al., The role of anthropogenic aerosol forcing in the 1850–1985 strengthening of the AMOC in CMIP6 historical simulations. *J. Clim.* **35**, 3243–3263 (2022).
70. JM Gregory, et al., Concepts and terminology for sea level: mean, variability and change, both local and global. *Surv. Geophys.* **40**, 1251–1289 (2019).
71. T Frederikse, et al., The causes of sea-level rise since 1900. *Nature* **584**, 393–397 (2020).